Nonlinear Analytical Modelling for Surface-Mounted Permanent Magnet Motors with Magnet Defect Fault

Zhaokai Li, Xiaoyan Huang, *Member, IEEE*, Yelong Yu, Dongdong Jiang, Lijian Wu, *Senior Member, IEEE,* and Tingna Shi, *Member, IEEE*

***Abstract*—This paper analyzes magnet defect fault signature in the surface-mounted permanent magnet motor (SPMM) using nonlinear analytical model considering the influence of magnet shape and magnetization direction. Based on the surface current method and conformal mapping technique, the magnet defect equivalent current and equivalent nonlinearity current are proposed to represent the magnet defect. Accordingly, the performance of SPMM can be obtained. The proposed model has great potential to investigate SPMM with non-uniform magnet defect and gives theoretical basis for fault diagnosis. The extra sensing coil is added to measure the voltage waveforms, which can also be predicted using the nonlinear analytical model and shows the influence of magnet defect fault. Finally, the finite element analysis and experimental results verify the high accuracy of nonlinear analytical model.**

***Index Terms*—Magnet defect, conformal mapping, magnetic circuit model, iron nonlinearity, surface-mounted permanent-magnet motors, fault signature.**

I. INTRODUCTION

THE PM motors have been increasingly used in many applications that require high efficiency and large power density. However, as the PMs are vulnerable and sensitive to mechanical shock, short circuit fault current and high temperature, the risk of magnet defect fault is high, making it one of major concerns for PM motors [1]-[12]. There are various methods to analyze the magnet defect fault of PM motors using sensing coil [2], hall sensor [3], back-EMF [4], stator current [5] or zero-sequence voltage [6]. In these methods, the accurate motor models are all required to establish the relationship between the magnet defect fault and the electromagnetic performance, which gives the criterion for judgement of magnet defect. They can also be used to improve the electromagnetic design of PM motors for reducing the risk of demagnetization [7]-[9] and check the demagnetization under short circuit fault [10]-[12].

The high calculation speed is also important for analyzing the PM motors with magnet defect fault as there are different kinds of magnet defect fault under various operating points in the real application. In order to distinguish the magnet defect faults and predict the fault severity, it is necessary to analyze all cases of one PM motor with different magnet defect faults and operating points. Although the fault diagnosis can be accurate and convincing in this way, it consumes too much computing time to obtain the comprehensive results. Hence, it is worthy to build an efficient and accurate motor model considering magnet defect fault.

Among the motor models, finite-element analysis (FEA) is the most widely-used method to analyze the performance of PM motor with magnet defect fault due to its high accuracy and it is suitable for any type of PM motor. Chen *et al.* investigated the anti-demagnetization capability of PM wind generator with different slot pole combination and rotor type [11]. Wu *et al.* analyzed the short current response under typical types of loads considering the demagnetization based on FEA and shows high accuracy with experimental results [12]. Li *et al.* found that flux gaps have significant impact on magnet demagnetization for SPMMs using FEA [13]. The detection of magnet defect faults through motor performance was also carried out based on the FEA results [14]-[15]. However, the FEA will consume much computing time.

The analytical model is alternative option for analysis of PM motors with magnet defect fault. It has great advantage of high efficiency with clear physical relationship between motor performance and the demagnetized or broken magnet. The conformal mapping [16] and subdomain model [17] can accurately and efficiently calculate the performance of surface-mounted PM motors under normal condition. Then the permeance function based on conformal mapping [18] or the subdomain model was improved to calculate the performance of axial-flux PM motors under magnet defect fault [19]. However, these analytical models neglect nonlinearity effect and show low accuracy at on-load condition [16]-[19]. The open-circuit performance of SPMM is analyzed considering rotor eccentricity, iron nonlinearity, and magnet defects based on combined subdomain and magnetic circuit model, but it doesn't account for the armature reaction [20].

The magnetic circuit model can consider iron nonlinearity for SPMM, but the calculation accuracy is greatly affected by the regularity of flux distribution and the size of magnetic reluctance. In [21], Mahmouditabar *et al.* proposed the demagnetization model of the axial-flux PM motors using magnetic equivalent circuit. In [22], Zafarani *et al.* proposed a

This work was supported in part by the National Natural Science Foundation of China (51922095) and the National Key R&D Program of China (2019YFE0123500). (Corresponding author: Xiaoyan Huang.)

The authors are with the Zhejiang Provincial Key Laboratory of Electrical Machine Systems, College of Electrical Engineering, Zhejiang University, Hangzhou, China (e-mail: xiaoyanhuang@zju.edu.cn).

magnetic equivalent circuit of SPMM to determine the influence of magnet defect faults based on frequency domain signature. Then, the motor topology is investigated under magnet defect fault at different operating points [23]. In [24]-[25], the magnetic circuit model is used to detect the magnet defect fault of PM motor. These models are fast compared with FEA, but their accuracy is not satisfactory due to coarse mesh for magnetic reluctance.

Recently, the hybrid analytical model based on either conformal mapping [26]-[27] or subdomain model [28]-[29] is used to investigate the electromagnetic performance of PM motors with the aid of magnetic circuit model considering nonlinearity effect. However, these models are not applicable to analyze those with magnet defect. Besides, the hybrid analytical models only consider the radial-sided magnet [30]-[31]. There is a paucity of literature on the analytical model of SPMM with parallel-sided magnet with parallel magnetization.

In this paper, a nonlinear analytical model (NAM) is proposed to investigate the characteristic of SPMM under magnet defect condition considering PM shapes, magnetization directions and iron nonlinearity. In the proposed model, the magnet defect equivalent current is introduced to represent the magnet defect fault severity. Meanwhile the fan-shaped magnet with radial magnetization and parallel-sided magnet with parallel magnetization in the SPMM are represented by the PM equivalent current. Moreover, the equivalent nonlinearity current is introduced on the interface between air region and iron region to account for iron nonlinearity. It is found that the variation of electromagnetic performance of SPMMs to magnet defect fault severity can be accurately and efficiently predicted using the proposed model. Hence, it is useful to analyze and extract the magnet defect fault signature. The FEA and experimental results are carried out to verify the proposed model.

II. Nonlinear Analytical Model for Magnet Defect

The magnet defect fault includes broken magnet or demagnetization, leading to the reduction of PM flux. When PM motors are operated under magnet defect fault, the winding current will be increased to obtain the same output torque. Under such circumstances, the iron nonlinearity is severe and cannot be neglected in order to guarantee the calculation accuracy of the analytical model. Besides, it is important for condition monitoring and fault diagnosis of SPMM to investigate the influence of PM shape and magnetization direction on the motor performance under magnet defect fault. In terms of these two issues, NAM is proposed to effectively predict the performance of SPMM accounting for PM shapes, magnetization directions and iron nonlinearity. The following assumptions are made for the model: 1) Linear property of PM with vacuum permeability; 2) negligible eddy current effect and end effect.

A. Magnet Defect Equivalent Current Transformation

In SPMMs, the rotor with fan-shaped and parallel-sided magnet are investigated considering magnetization direction, Figs. 1-2. Based on the surface current method, the PM equivalent current for the fan-shaped PM with radial magnetization is uniformly distributed at the two sides of magnet pole (line “1”and “2”) [19]. It is calculated by

$$i_{pm12} = \frac{H_{cj} h_m}{N_{PM}} \tag{1}$$

where H_{cj} and h_m are the coercivity and height of PM, respectively. N_{PM} is the number of PM equivalent current. In Fig. 1, N_{PM} represents the number of dot currents at one side of magnet and therefore N_{PM}=4. When the PM is partially demagnetized or broken, the magnet defect equivalent current occurs at two sides of the fault PM region (line “1”and “2”), as shown in Fig. 1(b) [19]. They are obtained using

$$i_{pm2} = \frac{(1-k_m) H_{cj} h_m}{N_{PM}} \tag{2}$$

$$i_{pm5} = \frac{k_m H_{cj} h_m}{N_{PM}} \tag{3}$$

where k_m is the ratio of the demagnetized flux density in the demagnetized PM to the residual flux density in the healthy PM. k_m=1 means full demagnetization of PM or broken PM and k_m=0 represents the healthy PM. In fact, the real shape for magnet defect can be irregular and the demagnetization usually occurs in the magnet corner. Under these circumstances, more division of PM is required for calculating the accurate value and position of PM equivalent current. Then, the total air-gap field with non-uniform demagnetization or breakage is calculated based on superposition principle. In order to show the effectiveness of the proposed model, this paper will focus on the uniformly partial demagnetization or damage in the PM for simplicity, but it is representative for PM defect fault.

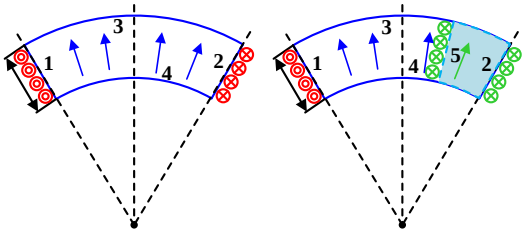

Fig. 1 The PM equivalent current for fan-shaped magnet under (a) normal condition and (b) defect fault condition.

For parallel-sided magnet with parallel magnetization, the PM equivalent current is required at every boundary of the PM region, Fig. 2(a). In the line “1”and “2”, the PM equivalent current producing the radial component of the parallel magnetization is expressed as

$$i_{pm12\_r}(R_d, \theta_m) = H_{cj} d_m(R_d, \theta_m) \cos^2(\theta_m) \tag{4}$$

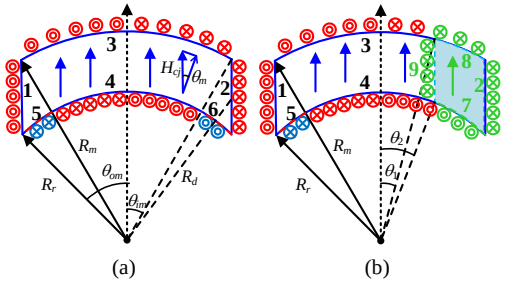

Fig. 2 The PM equivalent current for parallel-sided magnet under (a) normal condition and (b) defect fault condition.

where the dot current is located at (R_m, θ_m) in line "1" or "2" with the reference to PM center line. $d_m(R_m, \theta_m)$ is the thickness of PM corresponding to the dot current i_{pm12_r} in line "1" or "2". R_d is defined in Fig. 2(a).

In order to make the direction of PM magnetization parallel to the center line, the PM equivalent current in the outer and inner surface of PM should produce the specific tangential magnetization using geometric relationship. In the PM region between 0 and θ_{im}, the corresponding current at (R_m, θ_m) in curve "3"and at (R_r, θ_m) in curve "4" will produce the tangential component of the parallel magnetization. According to the vector synthesis method, the PM equivalent current can be expressed as

$$\begin{cases} i_{pm3\_c}(R_m,\theta_m) = H_{cj} R_m \theta_d \sin(\theta_m) \\ i_{pm4\_c}(R_r,\theta_m) = H_{cj} R_r \theta_d \sin(\theta_m) \end{cases} \tag{5}$$

where R_r and R_m are the inner and outer radii of the PM, respectively. θ_d is the angle corresponding to the uniformly distributed current. θ_{im} and θ_{im} are defined in Fig. 2(a).

As for the PM region between θ_{im} and θ_{om}, the tangential component of the parallel magnetization at (R_m, θ_m) comes from the PM equivalent current at (R_d, θ_m) in line "1" or "2" and at (R_r, θ_m) in dashed curve "5" or "6". Therefore, the currents can be calculated by

$$\begin{cases} i_{pm12\_c}(R_d,\theta_m) = H_{cj} d_m(R_d,\theta_m) \sin^2(\theta_m) \\ i_{pm56\_c}(R_r,\theta_m) = H_{cj} R_r \theta_d \sin(\theta_m) \end{cases} \tag{6}$$

According to (4) and (6), the total PM equivalent current at line "1"and "2" can be obtained using

$$\begin{aligned} i_{pm12}(R_d,\theta_m) &= i_{pm12\_r}(R_d,\theta_m) + i_{pm12\_c}(R_d,\theta_m) \\ &= H_{cj} d_m(R_d,\theta_m) \end{aligned} \tag{7}$$

When the PM is partially demagnetized or broken, the PM equivalent current at the line "2" and "9" is similar to that with radial magnetization and it is expressed as

$$\begin{cases} i_{pm2}(R_d,\theta_m) = (1-k_m) i_{pm12}(R_d,\theta_m) \\ i_{pm9}(R_d,\theta_m) = k_m H_{cj} d_f(R_d,\theta_m) \end{cases} \tag{8}$$

where $d_f(r,\theta)$ is the thickness of PM corresponding to the dot current i_{pm9_r}. Accordingly, the PM equivalent current at the line "8" is expressed as

$$i_{pm8\_c}(R_m,\theta_m) = (1-k_m) i_{pm3\_c}(R_m,\theta_m) \tag{9}$$

As for the PM equivalent current at the line "7", it will account for two kinds of magnet defect fault.

$$i_{pm7\_c}(R_r,\theta_m) = \begin{cases} (1-k_m) i_{pm56\_c}(R_r,\theta_m), & \theta_m \ge \theta_{im} \\ (1-k_m) i_{pm4\_c}(R_r,\theta_m), & \theta_m < \theta_{im} \end{cases} \tag{10}$$

B. Equivalent Nonlinearity Current Transformation

The iron nonlinearity is one of the key factors to decrease the output torque of SPMM besides the PM defect fault. Therefore, it is necessary to account for nonlinearity effect in the analytical model. The equivalence between the magnetic potential drop in the iron region and the surface current for iron nonlinearity on the boundary can be illustrated in Fig. 3. As the surface current sheet is used to represent the magnetic potential drop in the iron, the tangential iron permeability becomes infinite and therefore V_1'=V_2'. According to the Ampere's law, the equivalence between surface current and magnetic potential of iron can be expressed as

$$i_{iron} = -\frac{V_1 - V_2}{N_{iron}} \tag{11}$$

where i_{iron} is the value of single nonlinearity current. N_{iron} is the number of equivalent nonlinearity current corresponding to the tangential reluctance of iron. As shown in Fig. 3, N_{iron} represents the number of red currents which are uniformly distributed along the iron surface and therefore N_{iron}=3. As the iron region is considered to have infinite permeability, the analytical model is applicable to calculate the air-gap field. The radial flux which is obtained from the analytical model will flow into the iron and determines the iron field distribution based on the magnetic circuit theory.

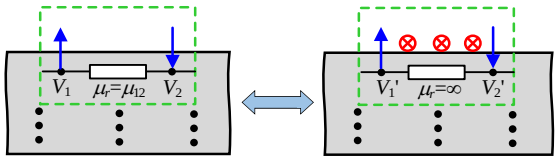

Fig. 3 Schematic view of equivalent nonlinearity current transformation

The general form of magnetic reluctance network (MRN) in the NAM can be simplified as one-slot/one-pole region, Fig. 4. For any slot pole combination, the MRN of slot and rotor region can be duplicated respectively. The magnetic flux source in the MRN can be obtained from the air-gap field distribution.

$$\phi_{rs} = l_{ef}\left[A_z(r_1,\alpha_1) - A_z(r_2,\alpha_2)\right] \tag{12}$$

where the magnetic vector potential A_z is located at (r_1,α_1) and (r_2,α_2) to obtain its corresponding value of flux source. l_{ef} is the effective length in SPMM.

In Fig. 4, there are two reluctances for stator yoke, two reluctances for stator tooth and three reluctances for tooth-tip in one-slot region. Besides, there are nine reluctances for rotor yoke in one-pole region. These reluctances for stator and rotor region are adequate to account for iron nonlinearity. If the nonlinearity level is much more severe than that in the conventional SPMMs, the reluctance number should be increased to obtain more accurate and detailed equivalent nonlinearity current.

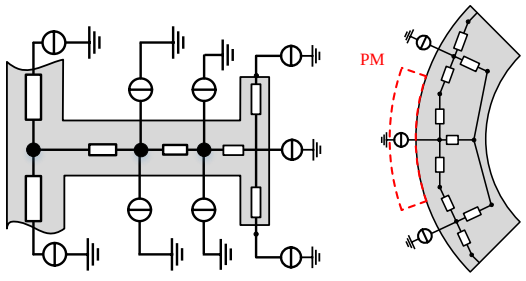

Fig. 4 The general MRN for (a) one-slot region and (b) one-pole region.

The winding current can be simplified as one dot current for single-layer winding or two dot currents for double-layer winding in each slot. It is located in the center of winding region and the corresponding value is expressed as

$$i_w = N_c i_{ph} \tag{13}$$

where i_{ph} is the value of phase current. N_c is the number of conductors for one coil. In this way, the proposed model is capable for analysing SPMM with any slot/pole combination and winding layout.

C. Conformal Mapping

The conformal mapping establishes the relationship of magnetic field between the slotted and slotless air-gap region. The analytical solution of radial and tangential flux density in the slotless air-gap is investigated in [32]. Three conformal mappings are required to obtain the slotted air-gap region, (14) -(16). Firstly, the logarithmic conformal mapping is used to transform the slotless air-gap annulus into the rectangular region. Then, the Schwarz-Christoffel (SC) mapping is required to convert the rectangle to the polygon. It is noted that the polygon is logarithmic solution of slotted air-gap region. Finally, the slotted air-gap region can be obtained using the exponential conformal mapping.

$$W = \frac{x_1}{2\pi}\left(\pi + j\log(\psi)\right) + j\frac{y_1}{2} \tag{14}$$

$$Z = A_0 \int \prod_{k=1}^{n-1} (W - w_k)^{-\frac{\beta_k}{\pi}} dW + C_0 \tag{15}$$

$$S = e^Z \tag{16}$$

where x_1 and y_1 are the rectangular width and height. A_0, C_0, β_k, w_k are the SC parameters [26]. In order to determine these parameters, the inverse form of these conformal mappings is derived to transform the slotted air-gap region into the slotless air-gap region. Consequently, the analytical solution of radial and tangential flux density B_r and B_α at (r,α) in the slotted air-gap can be expressed as

$$B_r = B_{r\psi}\lambda_a + B_{\alpha\psi}\lambda_b \tag{17}$$

$$B_\alpha = B_{\alpha\psi}\lambda_a - B_{r\psi}\lambda_b \tag{18}$$

where $B_{r\psi}$ and $B_{\alpha\psi}$ are the radial and tangential flux density in the slotless air-gap.

$$\lambda = \lambda_a + j\lambda_b = \left(\frac{\partial \psi}{\partial W}\right)^* \left(\frac{\partial W}{\partial Z}\right)^* \left(\frac{\partial Z}{\partial S}\right)^* \tag{19}$$

D. Nonlinear Solving Process

The NAM combines the linear analytical model (i.e., conformal mapping in this paper) with nonlinear MRN to consider both slotting effect and nonlinearity effect. It is impossible to directly obtain the value of equivalent nonlinearity current. The iterative calculation between the analytical model and MRN are used to obtain the nonlinear value. The total magnetic field is obtained according to the superposition principle.

Firstly, the magnetic potential of MRN based on Kirchhoff's voltage law can be simplified as

$$\begin{aligned} f(\mathbf{V}) &= \mathbf{A}\mathbf{\Lambda}\mathbf{A}^{\mathrm{T}}\mathbf{V} - (\mathbf{\Phi}_{\mathbf{PM}} + \mathbf{\Phi}_{\mathbf{iron}} + \mathbf{\Phi}_{\mathbf{Iw}}) \\ &= \mathbf{A}\mathbf{\Lambda}\mathbf{A}^{\mathrm{T}}\mathbf{V} - (\mathbf{K}_{\mathbf{PM}}\mathbf{I}_{\mathbf{PM}} + \mathbf{K}_{\mathbf{iron}}\mathbf{I}_{\mathbf{iron}} + \mathbf{K}_{\mathbf{Iw}}\mathbf{I}_{\mathbf{w}}) = 0 \end{aligned} \tag{20}$$

where $\mathbf{A}$ and $\mathbf{\Lambda}$ are the branch permeance matrix and node incidence matrix, respectively. $\mathbf{\Phi_{PM}}$, $\mathbf{\Phi_{iron}}$ and $\mathbf{\Phi_{Iw}}$ are the flux source matrix produced by PM equivalent current, equivalent nonlinearity current and winding current, respectively. $\mathbf{K_{PM}}$, $\mathbf{K_{iron}}$ and $\mathbf{K_{Iw}}$ are the coefficient matrix which is obtained from (12)-(19). $\mathbf{I_{PM}}$, $\mathbf{I_{iron}}$ and $\mathbf{I_w}$ represent the matrix of PM equivalent current i_{pm}, equivalent nonlinearity current i_{iron} and winding current i_w.

Then, the iterative calculation based on Newton-Raphson method is used to solve (20) and the magnetic field distribution of SPMM can be obtained at any rotor position. Finally, the electromagnetic performance of demagnetized SPMM can be analytically predicted, as shown in Fig. 5.

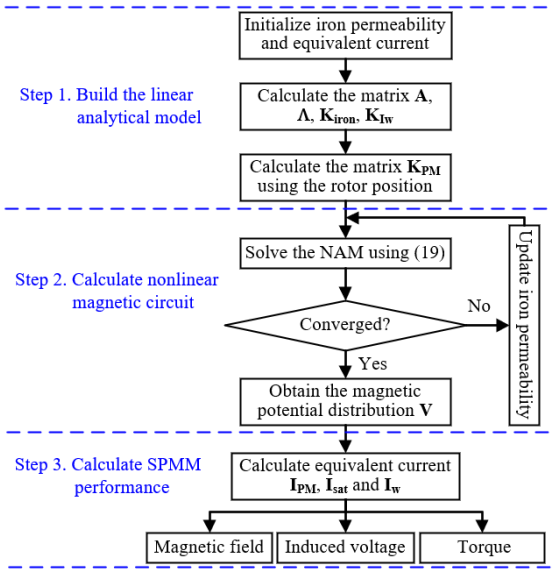

Fig. 5 The flowchart of solving process.

E. Motor Performance Calculation

The flux linkage of each phase can be obtained from the magnetic vector potential A_z for the coil.

$$\psi_{\text{phase}} = N_c \sum_{\tau} l_{ef}\left[A_z(r_{c\tau 1}, \alpha_{c\tau 1}) - A_z(r_{c\tau 2}, \alpha_{c\tau 2})\right] \tag{21}$$

where the coil is located at $(r_{c\tau 1}, \alpha_{c\tau 1})$ and $(r_{c\tau 2}, \alpha_{c\tau 2})$ belonging to the same phase. The induced phase voltage is obtained as

$$E_{phase} = -\frac{d\psi_{phase}}{dt} \tag{22}$$

The torque is calculated from the radial and tangential flux density based on Maxwell tensor theory.

$$T_e = \frac{r^2 l_{ef}}{\mu_0} \int_0^{2\pi} B_r(r,\alpha) B_\alpha(r,\alpha) d\alpha \tag{23}$$

III. Finite Element and Experimental Validation

Two 4-pole/24-slot SPMMs with fan-shaped PMs and parallel-sided PMs are designed and analyzed using JMAG, Fig. 6. They are assumed to have uniformly partial demagnetization or damage in one PM to verify the proposed model. The main parameters of the SPMMs are displayed in Table I. The rotor with parallel-sided PMs under uniformly partial damage is manufactured in Fig. 7 and the broken PM is indicated by the dotted circle. The aluminum can help install PM onto the rotor conveniently. It has negligible influence on the motor performance according to FEA. The back-EMF and torque of SPMM is measured using the test rig in Fig. 8.

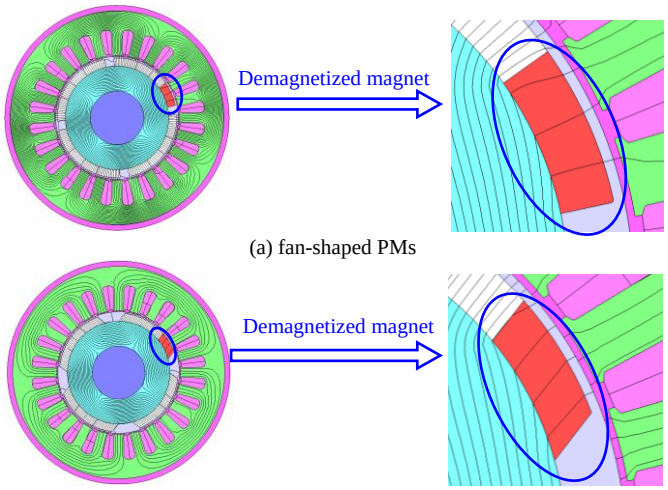

(a) fan-shaped PMs

(b) parallel-sided PMs

Fig. 6 The flux line distribution for SPMMs when k_m=0.75.

TABLE I
THE MAIN PARAMETERS OF SPMMS

Parameter	Fan-shaped PMs	Parallel-sided PMs
Stator outer diameter	120mm	
Stator inner diameter	70mm	
Slot opening	2.5mm	
Air-gap length	1.5mm	
Magnet height	4.5mm	
Iron material	B35A250	
Magnet angle/width	81°	35.1mm
Demagnetization angle/width	15°	11mm
DC voltage	150V	
Rated speed	3000rpm	

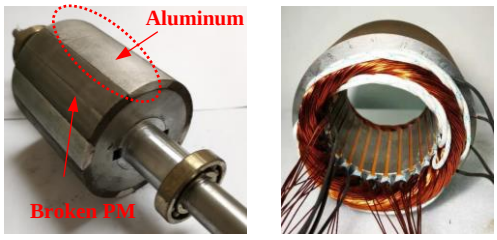

(a) Rotor (b) Stator

Fig. 7 The proptotype motor of SPMM with parallel-sided PMs when k_m=1.

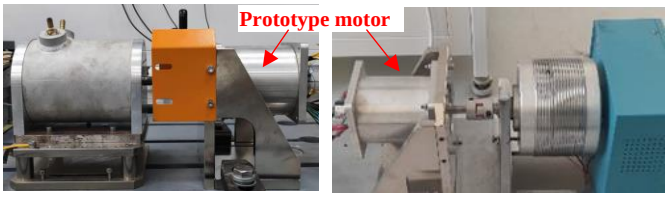

(a) motor drive system (b) powder dynamometer

Fig. 8 The test rig for meaturing the performance of prototype motor.

The air-gap field distribution of SPMM can be seen in Figs. 9-10. The broken magnet will significantly decrease the radial flux density and changed the value of tangential flux density in the defect region. Similar phenomenon can be seen in the variation of average flux density to the demagnetization ratio in Figs. 11-12, where the position range for calculating the average flux density is 10°-23° and 14.5°-39.5° for SPMM with fan-shaped PMs and parallel-sided PMs, respectively. As the demagnetization level goes higher (the demagnetization ratio k_m rises), the average radial flux density decreases due to the change of equivalent PM current in PM region.

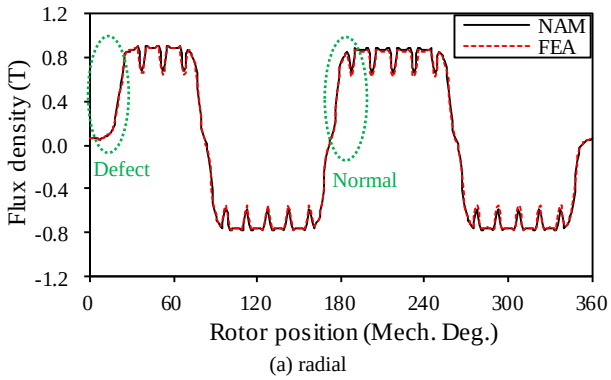

(a) radial

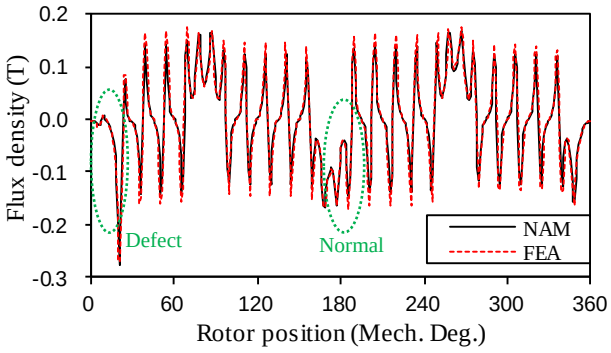

(b) tangential

Fig. 9 The air-gap field distribution of SPMM with fan-shaped PMs when k_m=1.

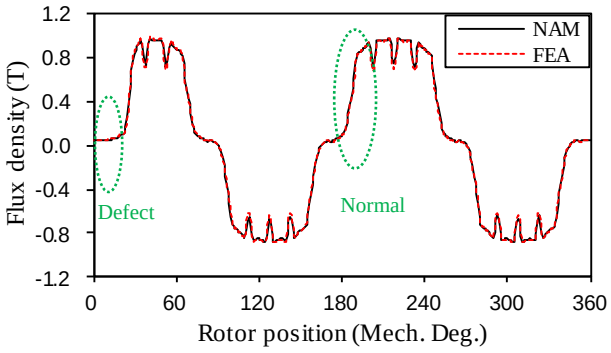

(a) radial

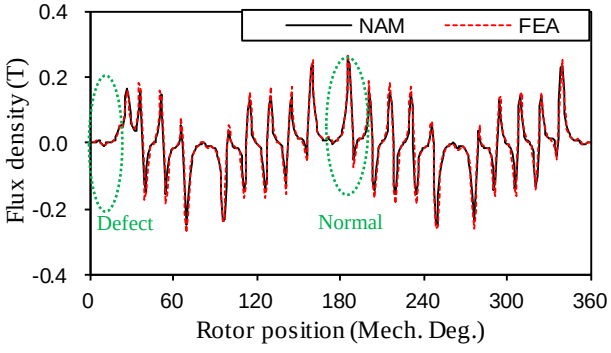

(b) tangential

Fig. 10 The air-gap field distribution of SPMM with parallel-sided PMs when k_m=1.

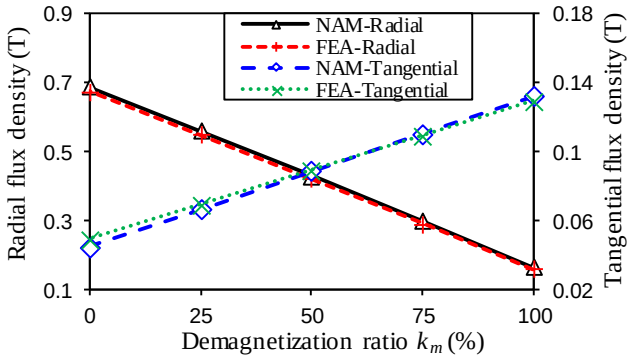

Fig. 11 The relationship between the average flux density and demagnetization ratio for SPMM with fan-shaped PMs under open-circuit condition.

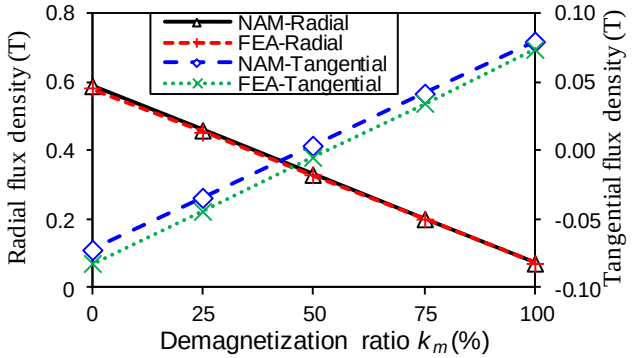

Fig. 12 The relationship between the average flux density and demagnetization ratio for SPMM with parallel-sided PMs under open-circuit condition.

Two kinds of sensing coils are arranged in the stator with coil span of one-slot and two-slot to analyze the demagnetization condition. NAM can accurately predict the voltage waveform of both sensing coils with high accuracy, Figs. 13-14. The NAM prediction of parallel-sided SPMM agrees well with measured coil voltage. As the span of two-slot is larger than the width between two PMs, the voltage waveforms of two-slot coil for both SPMMs are similar and they both have significant drop at the peak of coil voltage when facing the broken PM. As for one-slot coil voltage, the SPMM with fan-shaped PMs has peak voltage drop due to broken PM while the SPMM with parallel-sided PMs has wider gap between peak voltage facing the broken PM. Such difference mainly comes from the different pole-arc coefficient. If the width between PMs is smaller than one-slot span, the corresponding one-slot coil voltage is similar to that of the SPMM with fan-shaped PMs. Otherwise, it is similar to that of the SPMM with parallel-sided PMs.

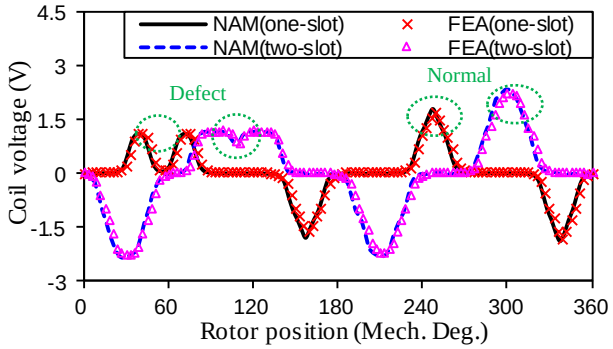

Fig. 13 The voltage waveform of (a) one-slot coil span and (b) two-slot coil span for SPMM with fan-shaped PMs when k_m=1.

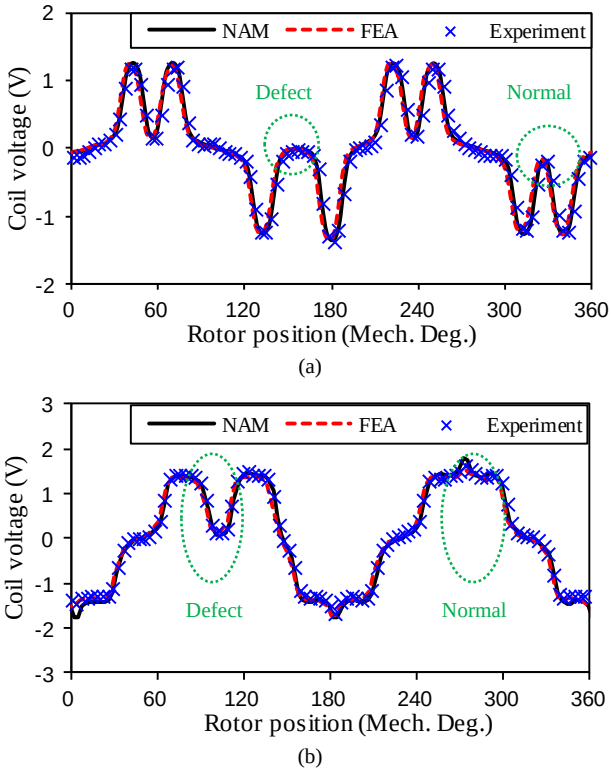

Fig. 14 The voltage waveform of (a) one-slot coil span and (b) two-slot coil span for SPMM with parallel-sided PMs when k_m=1.

The back-EMF predicted using NAM agrees well with FEA results for both SPMMs in Figs. 15-16. The experimental back-EMF for parallel-sided SPMM is also given in Fig. 16 and the errors of FEA calculation and NAM prediction are 4.8% and 2.7%, respectively. The causes of these errors are that the real PM remanence in the prototype is higher than the typical value which used in the FEA and NAM. In Figs. 17-18, when the demagnetization condition becomes worse (the demagnetization ratio k_m rises), the fundamental voltage under open-circuit condition decreases slightly, which is less than 7%. However, the 3rd harmonic voltage of SPMM with parallel-sided PMs at k_m=1 is 179% larger than that at k_m=0. The fan-shaped SPMM has 26% smaller 3rd harmonic voltage at k_m=1 than that at k_m=0. Hence, it is easier to analyze the demagnetization condition of SPMM using 3rd harmonic voltage ass one of the main magnet defect fault signatures.

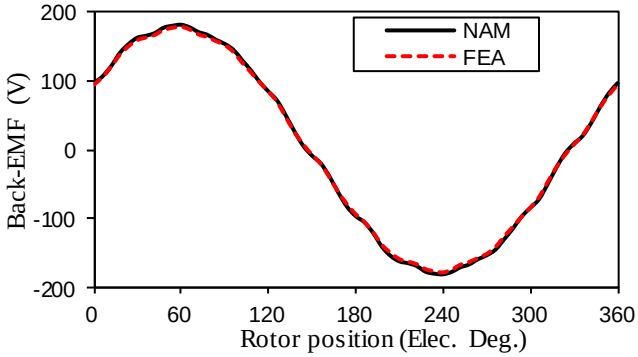

Fig. 15 The back-EMF waveform of SPMM with fan-shaped PMs when k_m=1.

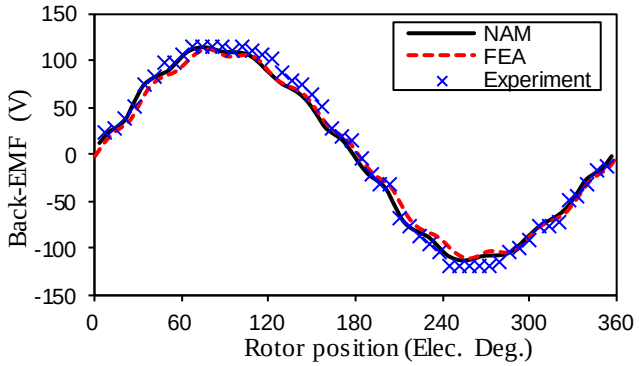

Fig. 16 The back-EMF waveform of SPMM with parallel-sided PMs when k_m=1.

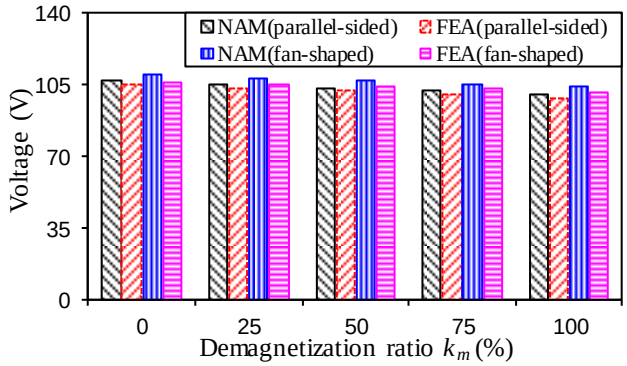

Fig. 17 The relationship between fundamental voltage and demagnetization ratio for SPMMs under open-circuit condition.

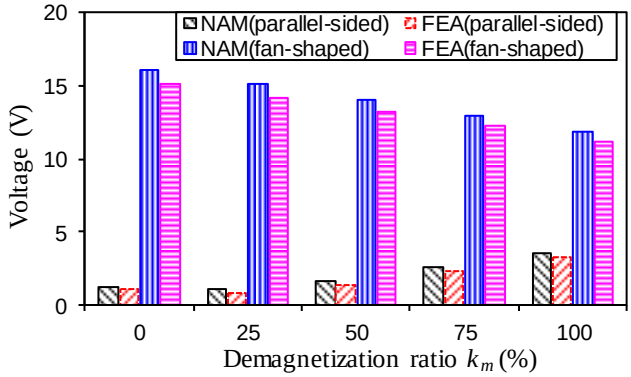

Fig. 18 The relationship between the 3rd harmonic voltage and demagnetization ratio for SPMMs under open-circuit condition.

The proposed model can accurately predict the cogging torque waveform under magnet defect, Figs. 19-20. The amplitude of the NAM prediction is slightly larger than the FEA results due to the simplification of iron modelling based on MRN and PM modelling using the equivalent current. Such errors are tolerable as the amplitude of cogging torque is already small enough and therefore the numerical errors are introduced in the calculation. In Figs. 21-22, when the demagnetization ratio grows, which means there is more severe demagnetization, the average torque decreases due to smaller PM flux linkage. The errors between the NAM and FEA are less than 3.9% for both motors at rated load. In Figs. 23-24, the SPMMs are operated with sinusoidal current source in FEA and NAM. The NAM predictions agree well with FEA results for both motors. Compared with experimental results in Fig. 24, FEA has the average errors of 8.5% while NAM has the average errors of 6.9%. The torque errors are larger than the back-EMF errors because the magnet defect fault will increase the harmonic component of winding current in the SPMM and introduce large errors.

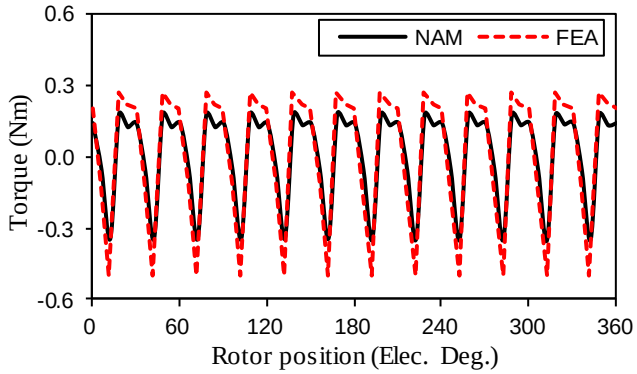

Fig. 19 The cogging torque waveform of SPMM with fan-shaped PMs when k_m=1.

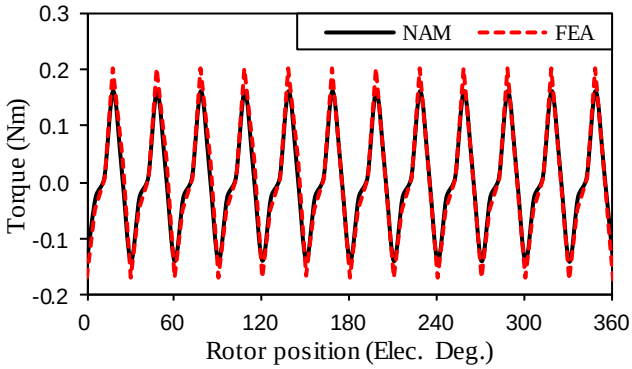

Fig. 20 The cogging torque waveform of SPMM with parallel-sided PMs when k_m=1.

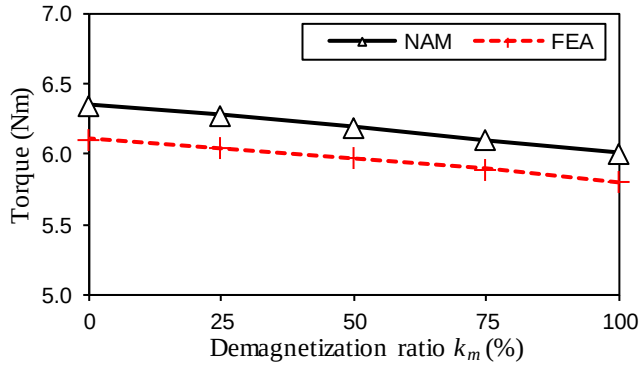

Fig. 21 The relationship between the average torque and demagnetization ratio for SPMM with fan-shaped PMs at rated load.

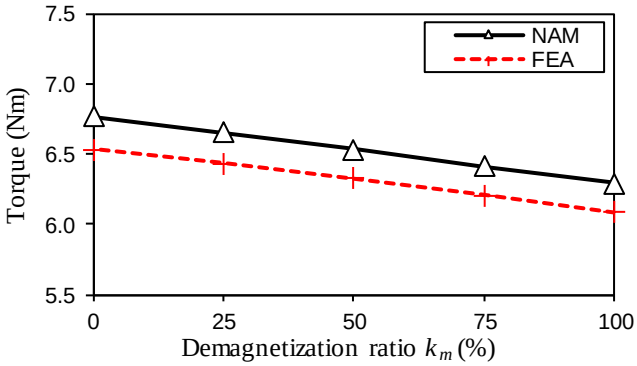

Fig. 22 The relationship between the average torque and demagnetization ratio for SPMM with parallel-sided PMs at rated load.

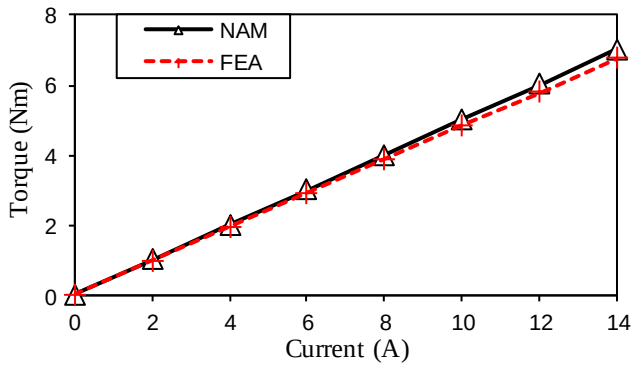

Fig. 23 The relationship between the average torque and the current for SPMM with fan-shaped PMs when k_m=1.

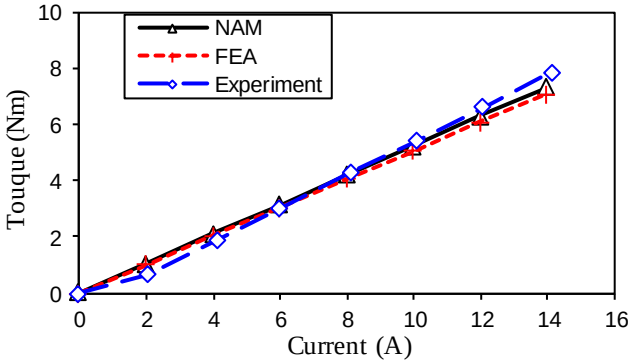

Fig. 24 The relationship between the average torque and the current for SPMM with parallel-sided PMs when k_m=1.

The comparison of calculation time for both motors using NAM and FEA is carried out in Table II. The NAM is running in the MATLAB and the FEA is utilized in the JMAG. It can be seen that the NAM can save over 88% and 60% the computational time of the FEA for fan-shaped and parallel-sided SPMM, respectively. The parallel-sided SPMM requires more calculation time since it has more PM equivalent current in the conformal mapping. It is concluded that the proposed model can analyze the demagnetization condition with less computing time. The calculation time of each step in Fig. 5 is also given in Table III for both motors at rated load. It can be seen that solving the nonlinear magnetic circuit consumes the most calculation time for NAM.

TABLE II
CALCULATION TIME OF NAM AND FEA AT RATED LOAD

SPMM	k_m	0	0.25	0.5	0.75	1
Fan-shaped	NAM (s)	31	45	45	56	44
	FEA (s)	481	491	515	513	530
Parallel-sided	NAM (s)	123	143	139	177	140
	FEA (s)	385	393	454	443	449

TABLE III
CALCULATION TIME OF EACH STEP IN NAM

Step	1	2	3
Fan-shaped SPMM (s)	6.1	35.8	2.1
Parallel-sided SPMM (s)	13.8	92.1	34.1

IV. CONCLUSION

In this paper, the nonlinear analytical model is proposed to analyze the fan-shaped and parallel-sided SPMMs under magnet defect fault considering iron nonlinearity. The magnet defect equivalent current is introduced to represent the partially demagnetized or broken PM with either radial or parallel magnetization accounting for the PM shape. Meanwhile, the equivalent nonlinearity current is proposed on the interface between the air region and iron region to account for the iron nonlinearity. It can be calculated from the magnetic potential distribution based on the nonlinear MRN. The iterative solving process is required to obtain the equivalent nonlinearity current. Therefore, the magnetic field is obtained by the superposition of PM equivalent current, magnet defect equivalent current, equivalent nonlinearity current, and winding current. The NAM can accurately predict the characteristic of the magnet defect fault from either the motor performance or the sensing coil. The high accuracy and high efficiency are verified by FEA for both motors. The experiment of parallel magnetized SPMM is carried out to validate the NAM for predicting the performance of parallel-sided SPMM with broken PM. The proposed model is also suitable to calculate the electromagnetic performance of axial-flux PM motors and the eddy current loss in segmented PMs of SPMM when the equation of eddy current loss is added to the model.

REFERENCES

[1] J. Faiz and E. Mazaheri-Tehrani, “Demagnetization modeling and fault diagnosing techniques in permanent magnet machines under stationary and nonstationary conditions: an overview,” *IEEE Trans. Ind. Appl.*, vol. 53, no. 3, pp. 2772-2785, May-June 2017.

[2] J. D. Bisschop, H. Vansompel, P. Sergeant, and L. Dupre, “Demagnetization fault detection in axial flux PM machines by using sensing coils and an analytical model,” *IEEE Trans. Magn.*, vol. 53, no. 6, pp. 1-4, Jun. 2017.

[3] Y. Park, D. Fernandez, S. Lee, D. Hyun, M. Jeong, S. Kommuri, C. Cho, D. Reigosa, and F. Briz, “Online detection of rotor eccentricity and demagnetization faults in PMSMS based on hall-effect field sensor measurements,” *IEEE Trans. Ind. Appl.*, vol. 55, no. 3, pp. 2499-2509, May-June 2019.

[4] L. Verkroost, J. De Bisschop, H. Vansompel, F. De Belie and P. Sergeant, “Active demagnetization fault compensation for axial flux permanent-magnet synchronous machines using an analytical inverse model,” *IEEE Trans. Energy Convers.*, vol. 35, no. 2, pp. 591-599, June 2020.

[5] M. Zafarani, T. Goktas, B. Akin and S. E. Fedigan, “Modeling and Dynamic behavior analysis of magnet defect signatures in permanent magnet synchronous motors,” *IEEE Trans. Ind. Appl.*, vol. 52, no. 5, pp. 3753-3762, Sept.-Oct. 2016.

[6] J. Urresty, J. Riba, M. Delgado and L. Romeral, "Detection of demagnetization faults in surface-mounted permanent magnet synchronous motors by means of the zero-sequence voltage component," *IEEE Trans. Energy Convers.*, vol. 27, no. 1, pp. 42-51, March 2012.

[7] T. Hosoi, H. Watanabe, K. Shima, T. Fukami, R. Hanaoka, and S. Takata, “Demagnetization analysis of additional permanent magnets in salient-pole synchronous machines with damper bars under sudden short circuits,” *IEEE Trans. Ind. Electron.*, vol. 59, no. 6, pp. 2448–2456, Jun. 2012.

[8] M. Kimiabeigi, J. D. Widmer, N. J. Baker, R. Martin, B. C. Mecrow, and A. Michaelides, "Three-dimensional modelling of demagnetization and utilization of poorer magnet materials for EV/HEV applications," *IEEE Trans. Energy Convers.*, vol. 31, no. 3, pp. 981-992, Sept. 2016.

[9] G. Choi and T. M. Jahns, “Analysis and design recommendations to mitigate demagnetization vulnerability in surface pm synchronous machines,” *IEEE Trans. Ind. Appl.*, vol. 54, no. 2, pp. 1292-1301, March-April 2018.

[10] Y. Du, L.J. Wu, H. Zhan and Y. Fang, "Influence of dimensional parameters on three-phase short circuit and demagnetization in surface-mounted pm machines," *IEEE Trans. Energy Convers.*, in press.

[11] H. Chen, R. Qu, J. Li and D. Li, "Demagnetization performance of a 7 MW interior permanent magnet wind generator with fractional-slot

concentrated windings," *IEEE Trans. Magn.*, vol. 51, no. 11, pp. 1-4, Nov. 2015.
[12] L. Wu, Y. Du, Z. Chen, Y. Guo, H. Wen and Y. Fang, "Influence of load characteristics on three-phase short circuit and demagnetization of surface-mounted PM synchronous motor," *IEEE Trans. Ind. Appl.*, vol. 56, no. 3, pp. 2427-2440, May-June 2020.
[13] G. J. Li, B. Ren, Z. Q. Zhu, M. P. Foster, and D. A. Stone, "Demagnetization withstand capability enhancement of surface mounted PM machines using stator modularity," *IEEE Trans. Ind. Appl.*, vol. 54, no. 2, pp. 1302-1311, March-April 2018.
[14] G. Kucukyildiz, E. Yolacan, H. Ocak and M. Aydin, "Detection of structural magnet defects for permanent magnet synchronous motors," *IEEE Trans. Energy Convers.*, in press.
[15] T. Goktas, M. Zafarani, K. W. Lee, B. Akin, and T. Sculley, "Comprehensive analysis of magnet defect fault monitoring through leakage flux," *IEEE Trans. Magn.*, vol. 53, no. 4, pp. 1-10, April 2017.
[16] D. Zarko, D. Ban, and T. A. Lipo, "Analytical solution for cogging torque in surface permanent-magnet motors using conformal mapping," *IEEE Trans. Magn.*, vol. 44, no. 1, pp. 52–65, Jan. 2008.
[17] L. J. Wu, Z. Q. Zhu, D. A. Staton, M. Popescu, and D. Hawkins, "Comparison of analytical models of cogging torque in surface-mounted pm machines," *IEEE Trans. Ind. Electron.*, vol. 59, no. 6, pp. 2414–2425, Jun. 2012.
[18] J. De Bisschop, P. Sergeant, A. Hemeida, H. Vansompel and L. Dupré, "Analytical model for combined study of magnet demagnetization and eccentricity defects in axial flux permanent magnet synchronous machines," *IEEE Trans. Magn.*, vol. 53, no. 9, pp. 1-12, Sept. 2017.
[19] B. Guo, Y. Huang, F. Peng, and J. Dong, "General analytical modeling for magnet demagnetization in surface mounted permanent magnet machines," *IEEE Trans. Ind. Electron.*, vol. 66, no. 8, pp. 5830–5838, Aug. 2019.
[20] W. Tong, S. Li, X. Pan, S. Wu and R. Tang, "Analytical model for cogging torque calculation in surface-mounted permanent magnet motors with rotor eccentricity and magnet defects," *IEEE Trans. Energy Convers.*, vol. 35, no. 4, pp. 2191-2200, Dec. 2020.
[21] F. Mahmouditabar, A. Vahedi, P. Ojaghlu, N. Takorabet, and A. Nobahari, "Demagnetization modelling of RWAFPM motor using magnetic equivalent circuit," 2019 19th International Symposium on Electromagnetic Fields in Mechatronics, Electrical and Electronic Engineering (ISEF), 2019, pp. 1-2.
[22] M. Zafarani, T. Goktas and B. Akin, "A comprehensive magnet defect fault analysis of permanent-magnet synchronous motors," *IEEE Trans. Ind. Appl.*, vol. 52, no. 2, pp. 1331-1339, March-April 2016.
[23] M. Zafarani, T. Goktas, B. Akin and S. E. Fedigan, "An investigation of motor topology impacts on magnet defect fault signatures," *IEEE Trans. Ind. Electron.*, vol. 64, no. 1, pp. 32-42, Jan. 2017.
[24] M. S. S. Rafaq et al., "Airgap search coil based identification of pm synchronous motor defects," *IEEE Trans. Ind. Electron.*, in press.
[25] Q. Xu, X. Liu, W. Miao, P. W. T. Pong and C. Liu, "Online Detecting Magnet Defect Fault in PMSG With Magnetic Sensing," *IEEE Trans. Transport. Electrific.*, vol. 7, no. 4, pp. 2775-2786, Dec. 2021.
[26] Z. Li, X. Huang, L.J. Wu, H. Zhang, T. Shi, Y. Yan, B. Shi, and G. Yang, "An improved hybrid field model for calculating on-load performance of interior permanent-magnet motors," *IEEE Trans. Ind. Electron.*, vol. 68, no. 10, pp. 9207–9217, Oct. 2021.
[27] L.J. Wu, Z. Li, D. Wang, H. Yin, X. Huang and Z.Q. Zhu, "On-load field prediction of surface-mounted PM machines considering nonlinearity based on hybrid field model," *IEEE Trans. Magn.*, vol. 55, no. 3, pp. 1-11, 2019.
[28] Y. Zhu, G. Liu, L. Xu, W. Zhao, and D. Cao, "A hybrid analytical model for permanent magnet vernier machines considering saturation effect," *IEEE Trans. Ind. Electron.*, in press, 2021.
[29] L.J. Wu, H. Yin, D. Wang, and Y. Fang, "On-load field prediction in SPM machines by a subdomain and magnetic circuit hybrid model," *IEEE Trans. Ind. Electron.*, vol. 67, no. 9, pp. 7190-7201, Sept. 2020.
[30] Y. Zhou, H. Li, G. Meng, S. Zhou, and Q. Cao, "Analytical calculation of magnetic field and cogging torque in surface-mounted permanent-magnet machines accounting for any eccentric rotor shape," *IEEE Trans. Ind. Electron.*, vol. 62, no. 6, pp. 3438–3447, Jun. 2015.
[31] L. Wu and Z. Zhu, "Analytical modeling of surface-mounted PM machines accounting for magnet shaping and varied magnet property distribution," *IEEE Trans. Magn.*, vol. 50, no. 7, pp. 1–11, Jul. 2014.
[32] B. Hague, "The principles of electromagnetism applied to electrical machines,", New York: Dover Publications, 1962.

Zhaokai Li was born in Lishui, China, in 1993. He received the B.S. degree and Ph.D. degree in electrical engineering from Zhejiang University, Hangzhou, China, in 2015 and 2020, respectively.

He is currently a postdoctoral researcher in Zhejiang University. His major research interests include the analytical modelling of PMSM and iron loss analysis.

Xiaoyan Huang (M'09) received the B.E. degree in control measurement techniques and instrumentation from Zhejiang University, Hangzhou, China, in 2003, and received the Ph.D. degree in electrical machines and drives from the University of Nottingham, Nottingham, U.K., in 2008.

From 2008 to 2009, she was a Research Fellow with the University of Nottingham. Currently, she is a professor with the College of Electrical Engineering, Zhejiang University, China, where she is working on electrical machines and drives. Her research interests are PM machines and drives for aerospace and traction applications, and generator system for urban networks.

Yelong Yu was born in Zhejiang, China, in 1995. He received the B.Eng. degree in electrical engineering in 2018 from Zhejiang University, Hangzhou, China, where he is currently working toward the Ph.D. degree in electrical engineering.

His research interests include the motor drive and control, and demagnetization fault diagnosis for permanent magnet synchronous motors.

Dongdong Jiang was born in Changzhou, China, in 1997. He received the B.S. degree in electrical engineering from Hebei University of Technology, Tianjin, China, in 2020.

Now he is working toward the master's degree in Zhejiang University, Hangzhou, China. His current major research interests include analysis, design and optimization of permanent magnet machines.

Lijian Wu (M'11-SM'14) received the B.Eng. and M.Sc. degrees from Hefei University of Technology, Hefei, China, in 2001 and 2004, respectively, and the Ph.D degree from the University of Sheffield, Sheffield, U.K., in 2011, all in electrical engineering.

From 2004 to 2007, he was an Engineer with Delta Electronics (Shanghai) Co, Ltd. From 2012 to 2013, he was with Sheffield Siemens Wind Power Research Center as a design engineer focusing on wind power generators. From 2013 to 2016, he was an advanced engineer with Siemens Wind Power A/S in Denmark. Since 2016, he has been with Zhejiang University, where he is currently Professor of electrical machines and control systems. His current major research interests include design and control of permanent magnet machines.

Tingna Shi (M'13) was born in Yuyao, China, in 1969. She received the B. S. and M. S. degrees from Zhejiang University, China, in 1991 and 1996 respectively, and the Ph.D. degree from Tianjin University, China, in 2009, all in electrical engineering.

She is currently a Professor with the College of Electrical Engineering, Zhejiang University, Hangzhou, China. Her current research interests include electrical machines and their control systems, power electronics, and electric drives.